When ellipsometry works best: a case study with transparent conductive oxides

HILLIER, James A. <http://orcid.org/0000-0002-3784-9337>, CAMELIO, Sophie <http://orcid.org/0000-0001-8484-2608>, CRANTON, Wayne <http://orcid.org/0000-0002-0142-7810>, NABOK, Alexei V., MELLOR, Christopher J., KOUTSOGEORGIS, Demosthenes C. and KALFAGIANNIS, Nikolaos <http://orcid.org/0000-0002-4030-5525>

Published version

HILLIER, James A., CAMELIO, Sophie, CRANTON, Wayne, NABOK, Alexei V., MELLOR, Christopher J., KOUTSOGEORGIS, Demosthenes C. and KALFAGIANNIS, Nikolaos (2020). When ellipsometry works best: a case study with transparent conductive oxides. ACS Photonics, 7 (10), 2692-2702.

Copyright and re-use policy

When Ellipsometry Works Best – A Case Study With Transparent Conductive Oxides.

*James A. Hillier, Sophie Camelio, Wayne Cranton, Alexei Nabok, Christopher J. Mellor, Demosthenes C. Koutsogeorgis, and Nikolaos Kalfagiannis**

KEYWORDS. Transparent Conductive Oxides, Spectroscopic Ellipsometry, Nano-photonics, Infrared Plasmonics, Dielectric function, Figures of Merit.

ABSTRACT

As the library of potential materials with plasmonic behaviour in the infrared (IR) grows, we must carefully assess their suitability for nano-photonic applications. This assessment relies on knowledge of the materials' optical constants, best determined *via* spectroscopic ellipsometry (SE). Transparent conductive oxides are great candidates for IR plasmonics due to their low carrier concentrations (compared to noble metals) and the ability to tailor their carrier concentration by manipulating the defect composition. When the carrier concentration becomes low enough, phonon and defect states become the dominant mechanism of absorption in the IR spectral range, leading to near-IR (NIR) tailing effects. These NIR tailing effects can be misinterpreted for free carrier absorption, rendering NIR-visible-ultraviolet-SE (NIR-VIS-UV-SE) incapable of reliably extracting the carrier transport properties. In this work, we report the precise limitations of NIR-VIS-UV and IR-SE (in terms of carrier concentration) by investigating the transport mechanisms

of indium tin oxide (ITO), aluminium-doped zinc oxide (AZO) and gallium-doped zinc oxide (GZO). We find that NIR-VIS-UV-SE fails for carrier concentrations below $(3.0 \pm 0.5) \times 10^{19}\, cm^{-3}$ for ITO, $(7 \pm 1) \times 10^{20}\, cm^{-3}$ for AZO and $(7 \pm 2) \times 10^{20}\, cm^{-3}$ for GZO. For IR-SE, the story is more complex and so we investigate the multi-faceted influences on the limitations, such as phonon behaviour, grain size, presence of a substrate, film thickness and measurement noise. Finally, we demonstrate the importance of identifying the IR optical constants directly *via* IR-SE (rather than by extrapolation from NIR-VIS-UV-SE) by means of comparing specific figures of merits (Joule and Faraday numbers), deemed useful indicators for plasmonic performance.

The promise of plasmonics is to usher in a new generation of opto-electronic devices through the exploitation of the strong interactions between light and free electrons at the nanoscale.[1,2] The free electrons oscillate in response to the electric field giving rise to surface plasmon polaritons (SPP) in planar metal/dielectric interfaces. Modern nanofabrication techniques have the ability to create metallic nanostructures which can confine light within dimensions far below the wavelength of light *via* excitation of localized surface plasmon resonances (LSPR).[3] By manipulating the nano-architecture, a wide variety of plasmonic responses have been demonstrated. Such architectures were able to advance applications in nanophotonics,[4–6] solar energy harvesting,[7,8] biosensing,[9,10] optical encoding,[11] photo-catalysis,[12,13] waveguiding[14] as well as the most impactful area of cancer treatment.[15,16]

The bulk of research into plasmonic device design has focused on the plethora of potential nano-architectures that can be utilized in order to either enhance the plasmonic performance for

particular applications or to tune the operational window towards unexplored spectral ranges. So far, the majority of research works utilize Au and Ag, which produce the strongest resonances due to their unrivalled conductivity.[17,18] However, this route has actually stalled the translation of these concepts into real and practical devices due to certain limitations of the noble metals, *i.e.* their incompatibility with CMOS techniques[19] and their low-melting point and high diffusivity (preventing their use at high-temperatures). Another key factor is that mono-atomic metals cannot be doped. Alloys can be made of different metals in order to tune the plasmon resonance, but such processes have limitations (i.e. ultrahigh doping challenges, interband transitions and degraded relaxation times).[20–23] As such, the operating frequency of a plasmonic nanostructure is generally tuned *via* varying the geometrical features (shape and size) as well as changing the local dielectric environment. This often causes compromises in their performance due to increased electronic losses at longer wavelengths.

Recently, focus has shifted towards alternative materials which overcome these limitations, including refractory metals,[24] transition metal nitrides,[25,26] and transparent conductive oxides (TCOs) such as tin-doped indium oxide (ITO), aluminium-doped zinc oxide (AZO) and gallium-doped zinc oxide (GZO).[27–29] The quest for alternative materials stems from the desire to expand the operational frequency without sacrificing performance. For example, extension of the resonance into the infrared (IR) can enable high-sensitivity label-free detection of molecules *via* vibrational/rotational spectroscopy.[17] At far IR and terahertz (THz) wavelengths, plasmonics has been proposed to benefit applications for photothermal detection, THz sources and imaging through opaque objects.[30] Vitally, the non-retarded frequency for plasmon resonance of nitrides and TCOs can be tuned through the manipulation of the defect composition[31,32] and application of an electric field *via* the Pockels effect.[33]

Materials with carrier concentrations below $\sim 10^{21}\ cm^{-3}$, such as TCOs, are appealing as active plasmonic elements in the IR regime. In order to assess their prospects, we require precise knowledge of the optical constants, taking into account the influence of optical phonons and/or defect states. Uprety and colleagues[34,35] previously demonstrated how IR spectroscopic ellipsometry (SE) is vital for gaining such knowledge. By simultaneously fitting SE data of ITO and AZO in the near-IR-visible-ultraviolet (NIR-VIS-UV) (0.75-5.89 eV), IR (0.035-0.4 eV) and THz (0.3-4.1 meV) regimes, they demonstrated how the NIR absorption should be interpreted as a combination of tailing effects from free carriers, phonons and/or low-energy defect states. They reported that fitting the NIR-VIS-UV resulted in overestimating the contribution of free carriers and that extension of the measured spectral range into the IR and THz regions produced greater agreement with 4-point probe measurements. In addition, Wang *et al.*[36] highlighted the requirement for extended frequency ranges to understand the conductivity of TCOs by noting how the presence of phonon modes in doped ZnO and ITO affect the measurement of the free electron relaxation.

Despite these findings, a large proportion of SE-based investigations of metal oxides still rely on SE in the NIR-VIS-UV and the use of IR-SE remains quite rare.[27,37–41] This reliance leads to false-positive results when it comes to metal oxides and other low carrier concentration materials, such as doped semiconductors. In this work, we examine a library of ITO, AZO and GZO sputtered films in order to assess the relationship between the carrier mobility and the carrier concentration elucidating the electron transport mechanisms (which define both plasmonic and electronic performance) *via* the different scattering regimes and non-parabolicity in the conduction band.[42–45] The knowledge generated in the present study expands further the findings of Uprety and colleagues[34,35] and Wang *et al.*[36] We demonstrate precisely when IR-SE measurements become

necessary for materials such as metal oxides. We find that IR-SE is vital for metal oxides with carrier concentrations below $(3.0 \pm 0.5) \times 10^{19}\, cm^{-3}$, $(7 \pm 1) \times 10^{20}\, cm^{-3}$ and $(7 \pm 2) \times 10^{20}\, cm^{-3}$ for ITO, AZO and GZO, respectively. We go further by considering the effects of inherent material limitations, noise and the presence of a substrate, across a wide range of carrier concentrations, in order to further elucidate the more complex limits that are encountered by IR-SE. Additionally, applying this knowledge we are able to present figures of merit (FoM) for two key potential plasmonic applications in the IR, namely the near-field enhancement and photothermal conversion, for ITO, AZO and GZO at the, currently un-reported, IR frequencies. This work will incentivize a reconsideration of strategies to unveil the origins of the features of the complex permittivity of alternative materials for IR plasmonics, such as oxides, nitrides and doped semiconductors.

RESULTS AND DISCUSSION

EXPERIMENTAL INVESTIGATION

A set of ITO, AZO and GZO thin films were fabricated *via* room temperature magnetron sputtering on top of test-grade n-type Si wafers (resistivity range: $1 - 20\ \Omega cm$). For each material, the deposition conditions were varied in order to produce films with similar crystal structure while covering a range of carrier concentrations. Further details on the experimental procedure and fabrication conditions can be found in the supporting information (SI), Section 1.1. The permittivity of each thin film was characterized *via* IR-SE. The permittivity is described by eq 1 as a summation of the high-frequency permittivity, ε_∞, a Drude term (describing free carrier absorption) and additional individual oscillators, $\tilde{\varepsilon}_n$.[46]

$$\tilde{\varepsilon}(E) = \varepsilon_\infty - \frac{\hbar^2}{\varepsilon_o \rho_{opt}\left(\tau_{opt} E^2 + i\hbar E\right)} + \sum_{n=1}^{m} \tilde{\varepsilon}_n(E) \qquad (1)$$

where $\hbar$ is the reduced Planck's constant, E is the photon energy, ε_0 is the vacuum permittivity, ρ_{opt} is the 'optical' resistivity and τ_{opt} is the 'optical' carrier mean free time. The third term represents a sum of m oscillators that describe phonon, defect state and interband absorption.

Further details of the SE equipment, fitting methodology and the individual oscillator functions can be found in the SI, Section 1.4. We follow the approach of Fujiwara *et al.,*[44] and others,[42,43,45] to consider the change in effective electron mass, m_e^*, with the carrier concentration, N, by taking into account the non-parabolicity of the conduction band as it is populated with free carriers. We do this by performing Hall Effect measurements which, when combined with IR-SE, allow us to directly calculate m_e^* for each sputtered thin film and determine how m_e^* varies with N, $m_e^*(N)$, for ITO, AZO and GZO. The $m_e^*(N)$ relationship is then utilized to calculate the carrier concentration and mobility, μ. This process is described in detail in the SI, Section 3. Figures 1a-c present the optical (green circles) and Hall (yellow squares) carrier concentration and mobility of the sputtered ITO, AZO and GZO films, respectively. The relationship between μ and N follows the trend described by Ellmer *et al.*[54] The $\mu(N)$ relationship is calculated for each material by following eqs 2-7 presented below. This approach accounts for the effects of grain boundary scattering (GBS) (*via* Seto's model)[55] and ionized impurity scattering (IIS) (*via* Masetti's model)[56] and ignores both dislocation scattering and neutral impurity scattering.

$$\frac{1}{\mu(N)} = \frac{1}{\mu_{IIS}(N)} + \frac{1}{\mu_{GBS}(N)} \qquad (2)$$

where:

$$\mu_{IIS}(N) = \mu_{min} + \frac{\mu_{max} - \mu_{min}}{1 + \left(\frac{N}{N_{ref1}}\right)^{\alpha_1}} - \frac{\mu_1}{1 + \left(\frac{N_{ref2}}{N}\right)^{\alpha_2}} \qquad (3)$$

$$\mu_{GBS}(N) = \mu_0(N) \cdot exp\left(-\frac{E_b(N)}{k_b T}\right) \qquad (4)$$

where k_b and T are the Boltzmann constant and temperature, respectively. μ_{max} is indicative of the lattice mobility, μ_{min} the ionised impurity inhibited mobility and $\mu_{min} - \mu_1$ of the ionised cluster inhibited mobility. N_{ref1} and α_1, are the transition concentration and coefficient, respectively, for ionized impurities while N_{ref2} and α_2 are the transition concentration and coefficient, respectively, for clusters of ionized impurities. $E_b(N)$ is the grain boundary height, for which the formulation changes depending on whether the grain is fully depleted and the traps are partially filled (eq 5), or the grain is partially depleted while the traps are fully filled (eq 6).[55]

$$E_b(N) = \frac{e^2 Q_t^2}{8\varepsilon_r \varepsilon_0 N}, \quad for \ \ LN > Q_t \qquad (5)$$

$$E_b(N) = \frac{e^2 L^2 N}{8\varepsilon_r \varepsilon_0}, \quad for \ \ LN < Q_t \qquad (6)$$

$$\mu_0(N) = \frac{eL}{\sqrt{2\pi \cdot m_e^*(N) \cdot k_b T}} \qquad (7)$$

where ε_0, ε_r, e, L and Q_t are the vacuum permittivity, static dielectric constant, elementary charge, grain size and trap density, respectively.

The $\mu(N)$ relationship as fitted to Hall Effect measurements of the sputtered TCOs is demonstrated with the black solid lines in Figure 1a-c. When fitting $\mu(N)$ to the experimental data only the parameters N_{ref2} and Q_t were left free, for AZO and GZO, with an additional requirement for α_2 as a free parameter for ITO. The parameters which influence $\mu(N)$ outside the experimental range were taken from Ellmer *et al.*,[57] where the experimental points covered a wider range of carrier concentrations. The input of grain size into eqs 6-7 was obtained *via* X-ray diffraction (see SI, Section 1.3). Table 1, below, outlines the parameters of $\mu(N)$ for each material.

Table 1. Fixed and free parameters of μ(N) for ITO, AZO and GZO.

Fixed Parameters	Unit	Material		
		ITO	AZO	GZO
μ_{max}	cm^2/Vs	210	210	210
μ_{min}	cm^2/Vs	55	55	55
$\mu_{min} - \mu_1$	cm^2/Vs	5	5	5
N_{ref1}	$\times 10^{17}\ cm^{-3}$	15	4	4
α_1		1	1	1
α_2		--	2	2
L	nm	5	25.6	52.1
ε_r		9	8.3	8.3
m_0^*		0.21± 0.02	0.24 ± 0.03	0.26 ± 0.02
C		0.4 ± 0.1	0.6 ± 0.2	0.6 ± 0.1
Free Parameters	Unit	Material		
		ITO	AZO	GZO
N_{ref2}	$\times 10^{20}\ cm^{-3}$	5.1 ± 0.3	1.2 ± 0.1	1.50 ± 0.05
α_2		14 ± 10	--	--
Q_t	$\times 10^{12}\ cm^{-2}$	3.7 ± 0.5	14.2 ± 0.5	27.0 ± 0.5

m_0^* and C describe how m_e^* changes with carrier concentration. They are extracted by fitting the set of Hall Effect and SE data presented in Figure 1a-c (see SI, Section 3).

The influence of the grain size on the $\mu(N)$ relationship is seen in Figures 1a-c. We first note a unique behavior for ITO, while some similarities are palpable for AZO and GZO. The most noticeable deviation between each material is in the region where GBS is dominant, which vastly inhibits the carrier mobility within the 'mobility hole' region. We highlight this region with the

yellow shaded area in Figures 1a-c. The boundaries of this region, with respect to N, result from L and Q_t (eqs 5-6).

Room temperature sputtered ITO thin films are nanocrystalline whereas sputtered AZO and GZO films follow a columnar structure with larger grains.[39] As the grain size increases, so does μ_0 (eq 7) and therefore the mobility at very low-N is larger. However, concurrently, the region where GBS becomes dominant covers a larger range of carrier concentrations. This is vital to consider for plasmonic material components, as materials with carrier concentrations within the GBS region will have poor ability to exploit plasmonic responses in the IR due to their inhibited carrier mobility. The onset of GBS with regard to N is defined by the trap density over the grain size,[54,58] so this limit may be reduced to lower carrier concentrations by reducing the trap density. This may be achieved by varying the growth conditions and/or following a post annealing process. Another option would be to take advantage of the ability of the high conductivity of amorphous ITO and IGZO films,[59,60] which negates the influence of GBS.[55] This is noted from Figure 1a where, for ITO, there is no region where $\mu \approx 0\ cm^2/Vs$.

In Figures 1b and 1c we observe few IR-SE experimental points ($N_{opt} = 8 \pm 1 \times 10^{19}\ cm^{-3}$ and $N_{opt} = 1.3 \pm 0.2 \times 10^{20}\ cm^{-3}$ for AZO and $N_{opt} = 1.0 \pm 0.1 \times 10^{20}\ cm^{-3}$ and $N_{opt} = 1.1 \pm 0.1 \times 10^{20}\ cm^{-3}$ for GZO) which deviate from the trend defined by the $\mu(N)$ relationship. Interestingly, these points do not agree with results from Hall Effect measurements (marked by red arrows in Figure 1b-c), even after corrections have been applied taking into account how m_e^* varies with N. Evidently, they produce erroneous values for m_e^* when evaluated against Hall Effect results (see SI, Section 3). For such points, N_{Hall} lies within the region of GBS. Based on the above understanding, we interpret that those results are invalid due to the diminished mobility invoked by GBS. To verify where precise determination of the transport properties is possible, for both IR

and NIR-VIS-UV-SE, we must already have precise knowledge of the carrier concentration and mobility. In addition, we need to go further down in carrier concentration values than the range covered by the experimental set of films in order to verify that SE becomes viable below the region of GBS. In response to these limitations, we performed the following ellipsometric theoretical experiment: we simulated the permittivity of ITO, AZO and GZO, extending the range of N covered by the experimental dataset while following careful rules that preserve the physical reality of such simulated datasets.

THEORETICAL INVESTIGATION

To produce the simulated data sets of the bulk permittivity, for each material, we vary the simulated carrier concentration, N_{sim}, between $10^{17} - 10^{21}\ cm^{-3}$. We calculate the simulated carrier mobility, μ_{sim}, from eqs 5-10, taking into account $m_e^*(N)$, and subsequently calculate ρ_{sim} and τ_{sim}. This brings the resistivity range between $10^{-4} - 10^{7}\ \Omega cm$. For each material, the contributions of IR and UV absorption are determined from fitting IR and NIR-VIS-UV-SE measurements of the film with a low carrier concentration (see SI, Section 5), so that the screening of the phonon and/or defect state absorption by the free carriers is minimized. The permittivity is built from the summation of the IR and UV oscillators of each material and the Drude term defined by ρ_{sim} and τ_{sim} for each simulated data set, as per eq 1. These steps, alongside those applied to establish $\mu(N)$ and $m_e^*(N)$, ensured that the simulated data are self-consistent. For every increment of N_{sim}, two distinct data sets are simulated, reflecting the ranges defined by two individual ellipsometers ($0.034 - 0.8\ eV$ for the IR and $0.775 - 6.5\ eV$ for the NIR-VIS-UV).

To elucidate the limitation of the capabilities of SE, in the different spectral ranges, we fit the simulated data sets using an identical model to the simulation (with all parameters left free) and record the 'optical' carrier concentration, N_{opt}, against N_{sim}. The results from fitting the NIR-

VIS-UV (blue squares) and IR (red circles) simulated data sets for ITO, AZO and GZO are presented in Figures 1d, 1e and 1f, respectively. The dashed black lines indicate the ideal case where $N_{opt} = N_{sim}$, which is valid for high enough carrier concentrations. As the carrier concentration decreases, we note three distinct areas where $N_{opt} \neq N_{sim}$. Each area is color coded in a way that we distinguish between different mechanisms. As the carrier concentration falls below a certain threshold (varied for each material) we notice that NIR-VIS-UV-SE (blue squares) deviates from the diagonal dashed line. This is indicated as the purple shaded areas in Figures 1d-f, where $N_{opt} \neq N_{sim}$ is exclusively due to NIR tailing effects (a NIR permittivity that resembles free electron absorption but is, instead, the result of additional oscillators in the IR). We define the limit of NIR-VIS-UV-SE as the point where the deviation between N_{opt} and N_{sim} is below 10%. For ITO this limit is found to be $(3.0 \pm 0.5) \times 10^{19}\ cm^{-3}$ (see SI, Section 4.4). However, the results from fitting the NIR-VIS-UV data sets maintain a negligible error in N_{opt}. This manifests a potential 'false positive' of NIR-VIS-UV-SE. At larger N, the free carrier absorption sufficiently screens the other contributions in the IR, ensuring a more accurate determination of the transport properties.

For the data sets simulated in the IR, a deviation from the diagonal dashed line, coupled with a significantly increased error bar, is noted for $N_{sim} \approx 10^{17}\ cm^{-3}$. This is indicated as the red shaded areas in Figure 1d-f, where $N_{opt} \neq N_{sim}$ is due to the 'IR detection limit'. This is a wavelength dependent limit that is due to rounding errors for simulated bulk films. For practical measurements the detection limit varies significantly due to a combination of the presence of noise (investigated by manually adjusting the noise in the data set), material/substrate reflections (investigated by simulating the film with varying thickness on a substrate) and/or IR absorption centers. Additionally, the IR detection limit can be reduced by utilizing films, substrates or optical

spacers with a thickness sufficient to produce interference effects within the measured spectral range. These effects are explored in more detail in the SI, Section 4.

For AZO (Figure 1e), the limit for inaccurate determination of the carrier concentration *via* NIR-VIS-UV-SE is higher (in terms of N) than for ITO (Figure 1d). Specifically, the threshold where N_{opt} is within 10% of N_{sim} is found to be $(7 \pm 1) \times 10^{20} cm^{-3}$. The NIR tailing effects for GZO are near identical to those for AZO (see SI, Section 5.2**)** and so we report an equal threshold of $(7 \pm 2) \times 10^{20} cm^{-3}$ (see SI, Section 4.4). To the best of our knowledge, a false-positive measurement of the carrier concentration of ITO *via* NIR-VIS-UV-SE has, as-of-yet, not been reported. This is likely because the most prominent implementation of TCOs has been electronic applications,[38–41] or plasmonics at the telecom wavelengths,[27,37] where larger carrier concentrations are desired. However, there is a collection of studies which extract the carrier transport properties of AZO and GZO from NIR-VIS-UV-SE or VIS-NIR reflection measurements while the carrier concentration is close-to or under the limit established in this work.[29,50,61–64] Furthermore, as the plasmonic community explores materials with lower N in order to exploit IR plasmonics, the requirement for IR-SE becomes even more pronounced.

An additional case where $N_{opt} \neq N_{sim}$ arises when fitting AZO in the IR. When $N_{sim} = 10^{18} - 10^{19.5}\ cm^{-3}$, N_{opt} is considerably underestimated and the error in N_{opt} is enormous (yellow shaded area in Figure 1e). This region directly overlaps the region where μ is diminished by the influence of GBS (yellow shaded area in Figure 1b). This diminished mobility produces an extremely damped Drude term which becomes undetectable within either (or in fact any) spectral windows. It is apparent that in order to determine the carrier concentration of a material *via* SE, the N must fall outside the window of GBS. It should be noted that the simulation has assumed that the grain size and trap density does not change with carrier concentration. Accounting for this

change would likely shift the low-N boundary for GBS (see SI, Section 3). However, if this boundary is higher than the detection limit of IR-SE ($\sim 10^{17}\ cm^{-3}$ in the presented cases), accurate determination of the transport properties is possible below the GBS threshold (see the point $N_{sim} = 10^{17.5}\ cm^{-3}$ in Figure 1e). We find similar results for GZO, with the exception that the window of GBS is large enough to overlap with the fundamental detection limits so that there is no region of $N_{opt} = N_{sim}$ below $10^{20.5}\ cm^{-3}$. The above-mentioned results have a prominent effect in the complex permittivity of the studied, sputtered, metal oxides. From the variety of samples presented above (Figures 1a-c) we choose two distinct thin films of each material that cover the experimental range of N. We denote these samples as 'low-N' and 'high-N' hereafter and in the SI. The permittivity of these samples was determined from both IR and NIR-VIS-UV-SE measurements. Specifically, the parameters which describe the film thickness, surface roughness, high-frequency permittivity, and interband transitions were determined from NIR-VIS-UV-SE and fixed during the fitting of IR-SE data. This 'fitting strategy' was deemed to provide the best agreement with alternative measurement techniques (reflectance spectroscopy, 4pp, atomic force microscopy, see SI, Section 2). The measurements, fit, graphical and parameterized permittivity of these samples can be found in the SI, Section 5.

In Figure 2, we present the (a-c) real, $\varepsilon_1(E)$, and (d-f) imaginary, $\varepsilon_2(E)$, permittivity of the ITO, AZO and GZO films, respectively. We present the results, for the low-N (dark colored lines) and high-N (light colored lines) films, from fitting IR (red lines) and NIR-VIS-UV-SE (blue lines) measurements separately. The requirement for the two additional oscillators in the IR for ITO was previously noted by Uprety *et al.*[34] They ascribed the peak at $0.045\ eV$ to Sn-O, Sn-O-Sn and In-O optical phonon modes and a broader peak at ~0.26 eV to Sn-OH and O-H stretching, present due to water molecules within the chamber during the initial stage of deposition. However, the

appearance of the broader peak at significantly lower energy ($\sim 0.13\ eV$) for this set of sputtered ITO films, alongside the observation that the energy of this peak changes with the films' carrier concentration (see SI, Section 5) suggests that the peak may instead be related to shallow defect states. For AZO and GZO, we again required two additional oscillators in the IR. The peak at $0.05\ eV$ is ascribed to a strong optical phonon absorption of ZnO.[47,48] However, we also note a large broad peak at $\sim 0.12\ eV$ which is not present for undoped ZnO. Uprety *et al.*[35] required two additional peaks at 0.11 eV and 0.16 eV to fit IR-SE measurements of AZO which they attributed to phonon modes. However, to the best of our knowledge, correlation of these peaks to Raman spectra is not possible due to the limited spectral range of current Raman analysis of undoped- and/or doped-ZnO.[47–50] It is of great interest to determine whether this peak is due to additional phonon modes caused by the presence of substitutional dopants, phonon-plasmon coupling,[51,52] defect-states or if it is an artefact arising from a non-uniform structure.[53] Determination of the precise mechanism behind this absorption is, however, beyond the scope of this work.

In addition to the permittivity, for each film in Figure 2, we present only the Drude term that was determined *via* IR-SE (dashed black lines) alongside the extrapolation of the NIR-VIS-UV permittivity into the IR (dashed blue lines). To highlight the effect of NIR tailing, we indicate the region between the measured permittivity and the expected permittivity, if only free carriers were present, by the purple shaded region. We note that the NIR tailing is more significant for the doped ZnO films than for ITO, due to the increased intensity of the absorption peak at ~0.12 eV. The increased tailing results in the higher value of N_{opt} when fitting the doped ZnO simulated data sets in the NIR-VIS-UV that is observed in Figures 1d-f. This, subsequently, results in a larger limit for accurate extraction of the carrier transport properties as a higher free carrier absorption is required to screen the tailing of the IR absorption.

The high-N ITO film is the only experimental material which shows no clearly visible NIR tailing and, therefore, IR and NIR-VIS-UV-SE agree to within 10% (Figure 1d). For the doped ZnO materials, we note that the absorption peak at $\sim 0.05\ eV$ results in a region of positive real permittivity for lower energies. This prevents any exploitation of plasmonic behavior in the far-IR. Conversely, for the low-N ITO, AZO and GZO films, the additional absorption peaks in the IR results in a window (or two distinct windows) of negative permittivity which is not present when only the free carrier absorption is considered. Therefore, exploitation of plasmonic (or in this case phononic) behavior is possible despite the insufficient conductivity.

FIGURES OF MERIT

A key result of the developed understanding of the requirements for IR-SE is that we are able to confidently expand the work of Lalisse *et al.*,[65] Doirion *et al.*,[66] and others[24,67–69] to accurately provide an array of useful figures of merit (FoMs) for key TCO material candidates with plasmonic responses in the IR. No plasmonic material is perfect and assessing the best material for each potential application is not trivial. To address this, the plasmonic community adopts universal dimensionless FoMs.[31,37,68] Two widely used FoMs evaluate the quality of both localized and propagating SPP, which are calculated from the $\varepsilon_1(E)$ and $\varepsilon_2(E)$. Lallise *et al.*[65] introduced two more useful FoMs, namely Faraday, Fa, and Joule, Jo, numbers which quantify the ability of a nanoparticle to enhance the optical near field and produce heat, respectively. These FoMs take into account the refractive index of the local dielectric medium and light source by introducing or removing a $1/n_s$ term in the Fa or Jo number, respectively. They drew up the values of the non-retarded resonance wavelength and Fa and Jo number at this wavelength for a large set of materials with plasmonic responses in the visible.

$$Fa(E) = |1 + 2\xi(E)|^2 \qquad (8)$$

$$Jo(E) = \frac{e\varepsilon_2(E)}{n_s}|\xi(E) - 1|^2 \qquad (9)$$

where n_s the refractive index of the surrounding medium and $\xi(E)$ is the enhancement factor, given by:

$$\xi(E) = \frac{\varepsilon_1(E) + i\varepsilon_2(E) - \varepsilon_M}{\varepsilon_1(E) + i\varepsilon_2(E) + 2\varepsilon_M} \qquad (10)$$

where ε_M is the permittivity of the local dielectric medium.

Figure 3 presents the (a) Faraday and (b) Joule numbers for ITO (green), AZO (blue) and GZO (red) thin films produced for this investigation. For comparison, we also present the values calculated for Ag (black), Al (dark grey), Au (light grey) and TiN (orange).[70,71] We also present the FoM for each material with a high (dark shade) and low (light shade) carrier concentration. In addition, Table 2 lays out the values of Fa and Jo at resonance alongside the screened plasma energy $E_{ps} = E(\varepsilon_1 = 0)$. Here, we show both the FoM resulting from fitting SE measurements in the IR (solid lines), alongside the FoM when extrapolating the optical constants from the fit in the NIR-VIS-UV (dashed lines).

Table 2. Near-field enhancement, Fa^0, and photothermal conversion, Jo^0, numerical figure of merits for the noble metals and sputtered films.

Material	E_{ps} / λ_{co}		λ_{res}^{Fa}		Fa^0	λ_{res}^{Jo}		Jo^0
	eV	μm	eV	μm		eV	μm	
Ag	4.74	0.262	3.45	0.359	107	3.49	0.355	49.9
Al	> 6.50	< 0.191	> 6.50	< 0.191	--	> 6.50	< 0.191	--
Au	> 6.50	< 0.191	2.35	0.528	17.8	> 6.50	< 0.191	--
TiN	2.56	0.484	2.12	0.585	13.4	2.42	0.512	5.26

$ITO_{High\ N}$	0.617	2.01	0.487	2.55	36.7	0.513	2.42	3.95
$ITO_{Low\ N}$	0.276	4.49	0.214	5.80	11.0	0.256	4.84	0.710
$AZO_{High\ N}$	0.550	2.25	0.423	2.93	11.4	0.492	2.52	1.60
$AZO_{Low\ N}$	0.359	3.45	0.281	4.41	8.14	0.359	3.45	0.740
$GZO_{High\ N}$	0.663	1.87	0.505	2.46	17.9	0.557	2.23	2.65
$GZO_{Low\ N}$	0.358	3.46	0.271	4.58	8.57	0.358	3.46	0.754

Fa and Jo numerical Figure of Merits are recorded at their respective resonance wavelengths, λ_{res}^{Fa} and λ_{res}^{Jo} in eV and μm. Also shown are the screened plasma energy (eV) / crossover wavelength (μm), E_{ps}/λ_{co}.

The Faraday number (Figure 3a) shows clear improvements of each TCO candidate for near-field enhancement in the IR where Au and TiN are ineffective due to the large electronic losses at these photon energies. In fact, within the non-retarded regime considered by these FoM, Au and TiN lack any plasmonic enhancement in the IR. Despite the additional oscillators for ITO, AZO and GZO having energy far below the resonance, the broad nature of these peaks strongly influence the Faraday number at resonance, resulting in a significant reduction in their predicted performance in comparison to that suggested from NIR-VIS-UV-SE alone. Specifically, by considering the IR during determination of the optical constants for the high-*N* ITO, GZO and AZO films, the FoMs for near-field enhancement (relative to the static case where $Fa = 9$) are reduced by 7%, 73% and 29%, respectively, from the NIR-VIS-UV result. For AZO and GZO, we also find that the resonance energy is blue-shifted due to the deviations revealed by IR-SE. When considering IR-SE we reveal that ITO provides the strongest un-retarded near-field enhancement out of the three key TCO candidates, largely due to its higher mobility. We observe similar results for the Joule number in Figure 3b. We present the FoMs for SPP, LSPR and the Mie absorption efficiency in the SI, Section 6.

CONCLUSIONS

To conclude, we have investigated the precise limitations of NIR-VIS-UV-SE and IR-SE, independently, to determine the free carrier transport properties and optical constants of key TCO material candidates for IR plasmonics. At first, we fabricated a large set of ITO, AZO and GZO thin films and characterized their transport properties, *via* SE and Hall Effect, to establish the relationship between the effective mass, carrier concentration and mobility for each material due to non-parabolicity in the conduction band and various scattering mechanisms. Importantly, we brought another perspective to the physical mechanisms behind the large broad peak in the IR for ITO, AZO and GZO. Furthermore, we found that the presence of GBS in doped ZnO can diminish the free carrier mobility, and thus the plasmonic 'quality', when the defects are manipulated to red-shift the plasma energy further into the IR.

We then utilized the established $\mu(N)$ and $m_e^*(N)$ relationships and ellipsometrically determined absorption centers to simulate a set of SE measurements covering a wide range of carrier concentrations for ITO, AZO and GZO. We demonstrated that there are three vital factors to consider clarifying when SE correctly determines the transport properties of low carrier concentration materials: NIR tailing, GBS and spectral sensitivity. By considering each case we can build confidence in material properties extracted *via* SE. For the TCO candidates investigated, we confirmed that the phonon and/or defect state absorption in the IR, for each material, has significant tailing into the NIR. This results in an overestimation of the Drude contribution to the permittivity in the NIR-VIS-UV. The free carrier absorption dominates the spectrum in the NIR, allowing for accurate determination of the carrier transport properties, at carrier concentrations of $(3.0 \pm 0.5) \times 10^{19}\, cm^{-3}$ for ITO, $(7 \pm 1) \times 10^{20}\, cm^{-3}$ for AZO and $(7 \pm 2) \times 10^{20}\, cm^{-3}$ for GZO. Below this threshold IR-SE measurements become of utmost importance. Moreover, we elucidated the more complex limits that are encountered by IR-SE by considering inherent material

limitations, measurement noise and the presence of a substrate, across a wide range of carrier concentrations. Vitally, the methodology outlined in this work can be applied to new materials to ensure confidence in measured and reported carrier transport properties determined *via* SE.

Finally, we demonstrated the importance of acquiring accurate measurements of the optical constants in the IR by expanding the library of FoMs for plasmonic applications to include the TCOs. We noted how measurements of the permittivity of TCOs *via* NIR-VIS-UV overestimates their plasmonic quality. We identified that the additional absorption in the IR prevent the exploitation of plasmonic phenomena in the far-IR but create pockets of negative real permittivity for metal oxide films with low conductivity, allowing for exploitation of phononic behavior in the IR.

ASSOCIATED CONTENT

Supporting Information. Materials and methods, fitting strategy, evaluation of $m_e^*(N)$, further ellipsometric limits (random noise, presence of a substrate, thickness, additional oscillators, case for experimental films), raw and fit ellipsometric measurements, optical constants, fitting parameters and additional figures of merit. This material is available free of charge *via* the Internet at http://pubs.acs.org.

AUTHOR INFORMATION

Corresponding Author

Nikolaos Kalfagiannis – Nottingham Trent University, School of Science and Technology, Nottingham, NG11 8NS, UK

Email: nikolaos.kalfagiannis@ntu.ac.uk

Authors

James A. Hillier – Nottingham Trent University, School of Science and Technology, Nottingham, NG11 8NS, UK

Sophie Camelio – Institut Pprime, UPR 3346 CNRS-Université de Poitiers, Poitiers, France

Wayne Cranton – Sheffield Hallam University, Materials and Engineering Research Institute, Sheffield, S1 1WB, UK

Alexei Nabok – Sheffield Hallam University, Materials and Engineering Research Institute, Sheffield, S1 1WB, UK

Christopher J. Mellor – The University of Nottingham, School of Physics and Astronomy, Nottingham, NG7 2RD, UK

Demosthenes C. Koutsogeorgis – Nottingham Trent University, School of Science and Technology, Nottingham, NG11 8NS, UK

Author Contributions

The manuscript was written through contributions of all authors. All authors have given approval to the final version of the manuscript.

Funding Sources

James A. Hillier acknowledges funding from the Nottingham Trent University Vice Chancellor's PhD Bursary Scheme.

Nikolaos Kalfagiannis acknowledges support from Nottingham Trent University, School of Science and Technology capital equipment funding scheme for acquiring the Infrared Spectroscopic Ellipsometry system.

Sophie Camelio acknowledges the “Région Nouvelle-Aquitaine” and the European Regional Development Fund (ERDF 2014-2020) for funding within the IMATOP Project No. P-2016-BAFE-209.Notes

ACKNOWLEDGMENT

The authors would like to acknowledge Joel Mohrmann, Ron Synowicki and Tom Tiwald from J. A. Woollam Co., Inc. for their insightful comments regarding this work.

ABBREVIATIONS

SPP, surface plasmon polaritons; LSPR, localized surface plasmon resonances; CMOS, complementary metal–oxide–semiconductor; TCO, transparent conductive oxide; ITO, tin-doped indium oxide; AZO, aluminium-doped zinc oxide; GZO, gallium-doped zinc oxide; IR, infrared; THz, terahertz; SE, spectroscopic ellipsometry; NIR-VIS-UV, near-infrared-visible-ultraviolet; FoM, figures of merit; SI, supporting information; IIS, ionized impurity scattering; GBS, grain boundary scattering; IGZO, indium-gallium-zinc-oxide.

REFERENCES

(1) Atwater, H. A.; Polman, A. Plasmonics for Improved Photovoltaic Devices. Nat. Mater. **2010**, 9 (3), 205–213.

(2) Brongersma, M. L.; Shalaev, V. M. The Case for Plasmonics. Science. **2010**, pp 440–441.

(3) Schuller, J. A.; Barnard, E. S.; Cai, W.; Jun, Y. C.; White, J. S.; Brongersma, M. L. Plasmonics for Extreme Light Concentration and Manipulation. Nat. Mater. **2010**, 9 (3), 193–204.

(4) Ozbay, E. Plasmonics: Merging Photonics and Electronics at Nanoscale Dimensions. Science. **2006**, pp 189–193.

(5) Gramotnev, D. K.; Bozhevolnyi, S. I. Plasmonics beyond the Diffraction Limit. Nat. Photonics **2010**, 4 (2), 83–91.

(6) Sun, K.; Xiao, W.; Ye, S.; Kalfagiannis, N.; Kiang, K. S.; Groot, C. H. (Kees.; Muskens, O. L. Embedded Metal Oxide Plasmonics Using Local Plasma Oxidation of AZO for Planar Metasurfaces. Adv. Mater. **2020**, 2001534.

(7) Boriskina, S. V.; Ghasemi, H.; Chen, G. Plasmonic Materials for Energy: From Physics to Applications. Mater. Today **2013**, 16 (10), 375–386.

(8) Boriskina, S. V.; Green, M. A.; Catchpole, K.; Yablonovitch, E.; Beard, M. C.; Okada, Y.; Lany, S.; Gershon, T.; Zakutayev, A.; Tahersima, M. H.; et al. Roadmap on Optical Energy Conversion. J. Opt. **2016**, 18 (7), 73004.

(9) Homola, J.; Yee, S. S.; Gauglitz, G. Surface Plasmon Resonance Sensors: Review. Sensors Actuators, B Chem. **1999**, 54 (1), 3–15.

(10) Mayer, K. M.; Hafner, J. H. Localized Surface Plasmon Resonance Sensors. Chem. Rev. **2011**, 111 (6), 3828–3857.

(11) Siozios, A.; Koutsogeorgis, D. C.; Lidorikis, E.; Dimitrakopulos, G. P.; Kehagias, T.; Zoubos, H.; Komninou, P.; Cranton, W. M.; Kosmidis, C.; Patsalas, P. Optical Encoding by Plasmon-Based Patterning: Hard and Inorganic Materials Become Photosensitive. Nano Lett. **2012**, 12 (1), 259–263.

(12) Pincella, F.; Isozaki, K.; Miki, K. A Visible Light-Driven Plasmonic Photocatalyst. Light Sci. Appl. **2014**, 3 (e113), 1–6.

(13) Martirez, J. M. P.; Carter, E. A. Prediction of a Low-Temperature N2 Dissociation Catalyst Exploiting near-IR-to-Visible Light Nanoplasmonics. Sci. Adv. **2017**, 3 (12), 1–11.

(14) Zenin, V. A.; Choudhury, S.; Saha, S.; Shalaev, V. M.; Boltasseva, A.; Bozhevolnyi, S. I. Hybrid Plasmonic Waveguides Formed by Metal Coating of Dielectric Ridges. Opt. Express **2017**, 25 (11), 12295.

(15) Lapotko, D. Plasmonic Nanobubbles as Tunable Cellular Probes for Cancer Theranostics. Cancers (Basel). **2011**, 3 (1), 802–840.

(16) Huang, X.; El-Sayed, M. A. Plasmonic Photo-Thermal Therapy (PPTT). Alexandria J. Med. **2011**, 47 (1), 1–9.

(17) Kim, S.; Kim, J. M.; Park, J. E.; Nam, J. M. Nonnoble-Metal-Based Plasmonic Nanomaterials: Recent Advances and Future Perspectives. Advanced Materials. **2018**, pp 1–24.

(18) Boltasseva, A.; Atwater, H. A. Low-Loss Plasmonic Metamaterials. Science. **2011**, 331 (6015), 290–291.

(19) Guler, U.; Kildishev, A. V.; Boltasseva, A.; Shalaev, V. M. Plasmonics on the Slope of Enlightenment: The Role of Transition Metal Nitrides. Faraday Discuss. **2015**, 178, 71–86.

(20) Blaber, M. G.; Arnold, M. D.; Ford, M. J. A Review of the Optical Properties of Alloys and Intermetallics for Plasmonics. J. Phys. Condens. Matter **2010**, 22 (14).

(21) Fafin, A.; Yazidi, S.; Camelio, S.; Babonneau, D. Near-Field Optical Properties of AgxAu1−x Nanoparticle Chains Embedded in a Dielectric Matrix. Plasmonics **2016**, 11 (5), 1407–1416.

(22) Rajendra, R.; Bhatia, P.; Justin, A.; Sharma, S.; Ballav, N. Homogeneously-Alloyed Gold-Silver Nanoparticles as per Feeding Moles. J. Phys. Chem. C **2015**, 119 (10), 5604–5613.

(23) Peña-Rodríguez, O.; Caro, M.; Rivera, A.; Olivares, J.; Perlado, J. M.; Caro, A. Optical Properties of Au-Ag Alloys: An Ellipsometric Study. Opt. Mater. Express **2014**, 4 (2), 403.

(24) Guler, U.; Shalaev, V. M.; Boltasseva, A. Nanoparticle Plasmonics: Going Practical with Transition Metal Nitrides. Mater. Today **2015**, 18 (4), 227–237.

(25) Patsalas, P.; Kalfagiannis, N.; Kassavetis, S.; Abadias, G.; Bellas, D. V.; Lekka, C.; Lidorikis, E. Conductive Nitrides: Growth Principles, Optical and Electronic Properties, and Their Perspectives in Photonics and Plasmonics. Mater. Sci. Eng. R Reports **2018**, 123, 1–55.

(26) Patsalas, P.; Kalfagiannis, N.; Kassavetis, S. Optical Properties and Plasmonic Performance of Titanium Nitride. Materials (Basel). **2015**, 8 (6), 3128–3154.

(27) Babicheva, V. E.; Kinsey, N.; Naik, G. V.; Ferrera, M.; Lavrinenko, A. V.; Shalaev, V. M.; Boltasseva, A. Towards CMOS-Compatible Nanophotonics: Ultra-Compact Modulators Using Alternative Plasmonic Materials. Opt. Express **2013**, 21 (22), 27326

(28) Zhong, Y.; Malagari, S. D.; Hamilton, T.; Wasserman, D. Review of Mid-Infrared Plasmonic Materials. J. Nanophotonics **2015**, 9 (1), 093791.

(29) Naik, G. V.; Shalaev, V. M.; Boltasseva, A. Alternative Plasmonic Materials: Beyond Gold and Silver. Adv. Mater. **2013**, 25 (24), 3264–3294.

(30) Caldwell, J. D.; Lindsay, L.; Giannini, V.; Vurgaftman, I.; Reinecke, T. L.; Maier, S. A.; Glembocki, O. J. Low-Loss, Infrared and Terahertz Nanophotonics Using Surface Phonon Polaritons. Nanophotonics **2015**, 4 (1), 44–68.

(31) Wang, Y.; Overvig, A. C.; Shrestha, S.; Zhang, R.; Wang, R.; Yu, N.; Dal Negro, L. Tunability of Indium Tin Oxide Materials for Mid-Infrared Plasmonics Applications. Opt. Mater. Express **2017**, 7 (8), 2727.

(32) Kanehara, M.; Koike, H.; Yoshinaga, T.; Teranishi, T. Indium Tin Oxide Nanoparticles with Compositionally Tunable Surface Plasmon Resonance Frequencies in the Near-IR Region. J. Am. Chem. Soc. **2009**, 131 (49), 17736–17737.

(33) Babicheva, V. E.; Boltasseva, A.; Lavrinenko, A. V. Transparent Conducting Oxides for Electro-Optical Plasmonic Modulators. Nanophotonics **2015**, 4 (1), 165–185.

(34) Uprety, P.; Junda, M. M.; Salmon, H.; Podraza, N. J. Understanding near Infrared Absorption in Tin Doped Indium Oxide Thin Films. J. Phys. D. Appl. Phys. **2018**, 51 (29).

(35) Uprety, P.; Junda, M. M.; Ghimire, K.; Adhikari, D.; Grice, C. R.; Podraza, N. J. Spectroscopic Ellipsometry Determination of Optical and Electrical Properties of Aluminum Doped Zinc Oxide. Appl. Surf. Sci. **2017**, 421, 852–858.

(36) Wang, T.; Zalkovskij, M.; Iwaszczuk, K.; Lavrinenko, A. V.; Naik, G. V.; Kim, J.; Boltasseva, A.; Jepsen, P. U. Ultrabroadband Terahertz Conductivity of Highly Doped ZnO and ITO. Opt. Mater. Express **2015**, 5 (3), 566.

(37) Noginov, M. A.; Gu, L.; Livenere, J.; Zhu, G.; Pradhan, A. K.; Mundle, R.; Bahoura, M.; Barnakov, Y. A.; Podolskiy, V. A. Transparent Conductive Oxides: Plasmonic Materials for Telecom Wavelengths. Appl. Phys. Lett. **2011**, 99 (2), 2–5.

(38) De Nicolás, S. M.; Muñoz, D.; Denis, C.; Lerat, J. F.; Emeraud, T. Optimisation of ITO by Excimer Laser Annealing for A-Si:H/c-Si Solar Cells. Energy Procedia **2012**, 27 (0), 586–591.

(39) El Hamali, S. O.; Cranton, W. M.; Kalfagiannis, N.; Hou, X.; Ranson, R.; Koutsogeorgis, D. C. Enhanced Electrical and Optical Properties of Room Temperature Deposited Aluminium Doped Zinc Oxide (AZO) Thin Films by Excimer Laser Annealing. Opt. Lasers Eng. **2016**, 80, 45–51.

(40) Liu, H.; Avrutin, V.; Izyumskaya, N.; Özgr, Ü.; Morkoç, H. Transparent Conducting Oxides for Electrode Applications in Light Emitting and Absorbing Devices. Superlattices Microstruct. **2010**, 48 (5), 458–484.

(41) Exarhos, G. J.; Zhou, X. D. Discovery-Based Design of Transparent Conducting Oxide Films. Thin Solid Films **2007**, 515 (18), 7025–7052.

(42) Romanyuk, V.; Dmitruk, N.; Karpyna, V.; Lashkarev, G.; Popovych, V.; Dranchuk, M.; Pietruszka, R.; Godlewski, M.; Dovbeshko, G.; Timofeeva, I.; et al. Optical and Electrical Properties of Highly Doped ZnO:Al Films Deposited by Atomic Layer Deposition on Si Substrates in Visible and near Infrared Region. Acta Phys. Pol. A **2016**, 129 (1), A36–A40.

(43) Liu, X.; Park, J.; Kang, J. H.; Yuan, H.; Cui, Y.; Hwang, H. Y.; Brongersma, M. L. Quantification and Impact of Nonparabolicity of the Conduction Band of Indium Tin Oxide on Its Plasmonic Properties. Appl. Phys. Lett. **2014**, 105 (18).

(44) Fujiwara, H.; Kondo, M. Effects of Carrier Concentration on the Dielectric Function of ZnO:Ga and In 2O 3:Sn Studied by Spectroscopic Ellipsometry: Analysis of Free-Carrier and Band-Edge Absorption. Phys. Rev. B - Condens. Matter Mater. Phys. **2005**, 71 (7), 1–10.

(45) Feneberg, M.; Nixdorf, J.; Lidig, C.; Goldhahn, R.; Galazka, Z.; Bierwagen, O.; Speck, J. S. Many-Electron Effects on the Dielectric Function of Cubic In2 O3: Effective Electron Mass, Band Nonparabolicity, Band Gap Renormalization, and Burstein-Moss Shift. Phys. Rev. B **2016**, 93 (4).

(46) De Sousa Meneses, D.; Malki, M.; Echegut, P. Structure and Lattice Dynamics of Binary Lead Silicate Glasses Investigated by Infrared Spectroscopy. J. Non. Cryst. Solids **2006**, 352 (8), 769–776.

(47) Huang, Y.; Liu, M.; Li, Z.; Zeng, Y.; Liu, S. Raman Spectroscopy Study of ZnO-Based Ceramic Films Fabricated by Novel Sol-Gel Process. Mater. Sci. Eng. B Solid-State Mater. Adv. Technol. **2003**, 97 (2), 111–116.

(48) Bundesmann, C.; Ashkenov, N.; Schubert, M.; Spemann, D.; Butz, T.; Kaidashev, E. M.; Lorenz, M.; Grundmann, M. Raman Scattering in ZnO Thin Films Doped with Fe, Sb, Al, Ga, and Li. Appl. Phys. Lett. **2003**, 83 (10), 1974–1976.

(49) Ashkenov, N.; Mbenkum, B. N.; Bundesmann, C.; Riede, V.; Lorenz, M.; Spemann, D.; Kaidashev, E. M.; Kasic, A.; Schubert, M.; Grundmann, M.; et al. Infrared Dielectric Functions and Phonon Modes of High-Quality ZnO Films. J. Appl. Phys. **2003**, 93 (1), 126–133.

(50) Zheng, H.; Zhang, R. J.; Li, D. H.; Chen, X.; Wang, S. Y.; Zheng, Y. X.; Li, M. J.; Hu, Z. G.; Dai, N.; Chen, L. Y. Optical Properties of Al-Doped ZnO Films in the Infrared Region and Their Absorption Applications. Nanoscale Res. Lett. **2018**, 13.

(51) Zollner, S.; Paradis, P. P.; Abadizaman, F.; Samarasingha, N. S. Drude and Kukharskii Mobility of Doped Semiconductors Extracted from Fourier-Transform Infrared Ellipsometry Spectra. J. Vac. Sci. Technol. B **2019**, 37 (1), 012904.

(52) Kukharskii, A. A. Plasmon-Phonon Coupling in GaAs. Solid State Commun. **1973**, 13 (11), 1761–1765.

(53) Özgür, Ü.; Alivov, Y. I.; Liu, C.; Teke, A.; Reshchikov, M. A.; Doğan, S.; Avrutin, V.; Cho, S. J.; Morkç, H. A Comprehensive Review of ZnO Materials and Devices. J. Appl. Phys. **2005**, 98 (4), 1–103.

(54) Ellmer, K.; Mientus, R. Carrier Transport in Polycrystalline Transparent Conductive Oxides: A Comparative Study of Zinc Oxide and Indium Oxide. Thin Solid Films **2008**, 516 (14), 4620–4627.

(55) Seto, J. Y. W. The Electrical Properties of Polycrystalline Silicon Films. J. Appl. Phys. **1975**, 46 (12), 5247–5254.

(56) Masetti, G.; Severi, M.; Solmi, S. Modeling of Carrier Mobility Against Carrier Concentration in Arsenic-, Phosphorus-, and Boron-Doped Silicon. IEEE Trans. Electron Devices **1983**, 30 (7), 764–769.

(57) Ellmer, K.; Mientus, R. Carrier Transport in Polycrystalline ITO and ZnO:Al II: The Influence of Grain Barriers and Boundaries. Thin Solid Films **2008**, 516 (17), 5829–5835.

(58) Frischbier, M. V.; Wardenga, H. F.; Weidner, M.; Bierwagen, O.; Jia, J.; Shigesato, Y.; Klein, A. Influence of Dopant Species and Concentration on Grain Boundary Scattering in Degenerately Doped In2O3 Thin Films. Thin Solid Films **2016**, 614, 62–68.

(59) Teixeira, V.; Cui, H. N.; Meng, L. J.; Fortunato, E.; Martins, R. Amorphous ITO Thin Films Prepared by DC Sputtering for Electrochromic Applications. Thin Solid Films **2002**, 420–421, 70–75.

(60) Ginley, D. S. Handbook of Transparent Conductors; Ginley, D. S., Hosono, H., Paine, D. C., Eds.; Springer: New York, USA, **2011**.

(61) Kim, H.; Osofsky, M.; Prokes, S. M.; Glembocki, O. J.; Piqué, A. Optimization of Al-Doped ZnO Films for Low Loss Plasmonic Materials at Telecommunication Wavelengths. Appl. Phys. Lett. **2013**, 102 (17), 1–5.

(62) Kim, J.; Naik, G. V.; Emani, N. K.; Guler, U.; Boltasseva, A. Plasmonic Resonances in Nanostructured Transparent Conducting Oxide Films. IEEE J. Sel. Top. Quantum Electron. **2013**, 19 (3).

(63) Xiao, S.; Drachev, V. P.; Kildishev, A. V.; Ni, X.; Chettiar, U. K.; Yuan, H. K.; Shalaev, V. M. Loss-Free and Active Optical Negative-Index Metamaterials. Nature **2010**, 466 (7307), 735–738.

(64) Naik, G. V.; Liu, J.; Kildishev, A. V.; Shalaev, V. M.; Boltasseva, A. Demonstration of Al:ZnO as a Plasmonic Component for near-Infrared Metamaterials. Proc. Natl. Acad. Sci. U. S. A. **2012**, 109 (23), 8834–8838.

(65) Lalisse, A.; Tessier, G.; Plain, J.; Baffou, G. Quantifying the Efficiency of Plasmonic Materials for Near-Field Enhancement and Photothermal Conversion. J. Phys. Chem. C **2015**, 119 (45), 25518–25528.

(66) Doiron, B.; Mota, M.; Wells, M. P.; Bower, R.; Mihai, A.; Li, Y.; Cohen, L. F.; Alford, N. M. N.; Petrov, P. K.; Oulton, R. F.; et al. Quantifying Figures of Merit for Localized Surface Plasmon Resonance Applications: A Materials Survey. ACS Photonics. **2019**, pp 240–259.

(67) Khurgin, J. B. Relative Merits of Phononics vs. Plasmonics: The Energy Balance Approach. Nanophotonics **2018**, 7 (1), 305–316.

(68) Berini, P. Figures of Merit for Surface Plasmon Waveguides. Opt. Express **2006**, 14 (26), 13030.

(69) Manjavacas, A.; Liu, J. G.; Kulkarni, V.; Nordlander, P. Plasmon-Induced Hot Carriers in Metallic Nanoparticles. ACS Nano **2014**, 8 (8),

(70) Palik, E. D. Handbook of Optical Constants of Solids; Academic Press: San Diego, CA, **2012**;

(71) Patsalas, P.; Logothetidis, S. Optical, Electronic, and Transport Properties of Nanocrystalline Titanium Nitride Thin Films. J. Appl. Phys. **2001**, 90 (9), 4725–4734.

LIST OF FIGURE CAPTIONS

Figure 1. (a-c) Carrier concentration and mobility of sputtered ITO, AZO and GZO films, respectively, as determined by IR-SE (green circles) and Hall Effect (yellow squares). The fit of $\mu(N)$ (eqs 2-7) to the Hall Effect measurements is shown by the black solid line. We highlight the regions where different scattering mechanisms are dominant with the different colors. (d-f) 'Optical' carrier concentration, N_{opt}, as determined by fitting each simulated dataset of N_{sim} for ITO, AZO and GZO, respectively. We show the result from fitting the data simulated in the IR (red circles) and in the NIR-VIS-UV (blue squares) alongside $N_{opt} = N_{sim}$ (black dashed diagonal line). The influence of the NIR tailing and GBS are indicated by the purple and yellow shaded areas, respectively.

Figure 2. (a-c) Real, $\varepsilon_1(E)$, and (d-f) imaginary, $\varepsilon_2(E)$, parts of the complex permittivity for the sputtered ITO, AZO and GZO films, respectively, as fit in the IR (solid red lines), as fit in the NIR-VIS-UV (solid blue lines), *via* extrapolation of the NIR-VIS-UV into the IR (dashed blue lines), and as simulated with only the Drude term of the IR fitted (dashed black/grey lines). 'Low-N' (darker lines) and 'High-N' (lighter lines) represent two distinct films of each material which cover the experimental range of carrier concentration. The purple shaded region highlights the difference between the simulated and fitted Drude contribution in the NIR, where tailing effects of the IR absorption centers are mistaken for free carrier absorption when fitting in the NIR-VIS-UV. Please note the changes in scale at -17 and 7 for the real permittivity and at 3 for the imaginary permittivity.

Figure 3. (a) Faraday and (b) Joule numbers for a TCOs alongside Ag, Al, Au and TiN for comparison. For the TCOs, the solid lines represent the 'true' FoM taking into account phonon and interband transitions and the dotted lines are the calculations employing extrapolated optical constants from NIR-VIS-UV-SE. Please note the change in scale in photon energy at $0.1\ eV$ and $0.7\ eV$ and the change in scale in the Faraday number at 10.

Figure 1

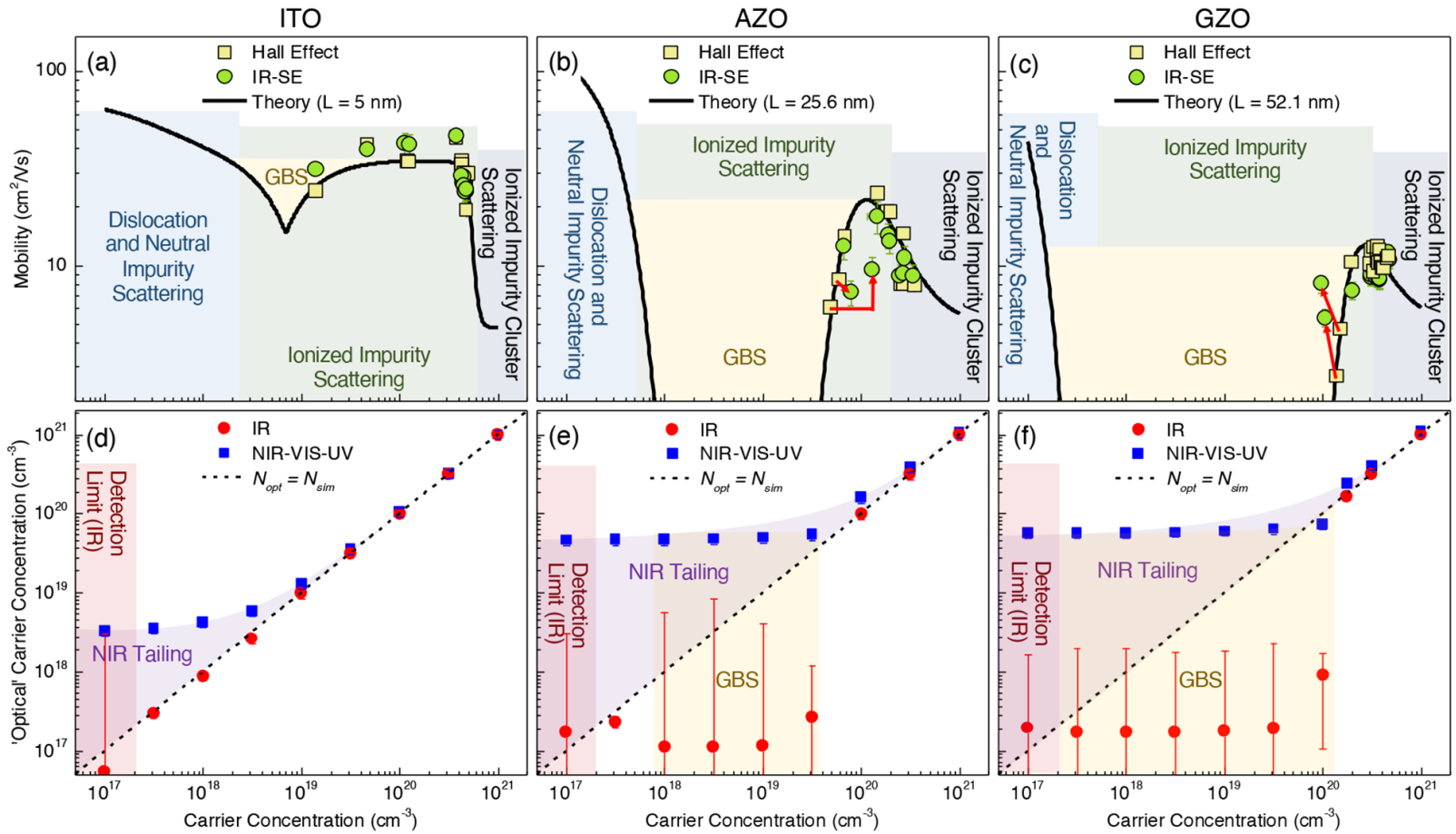
ITO
AZO
GZO
(a)
(b)
(c)
Hall Effect
IR-SE
Theory (L = 5 nm)
Theory (L = 25.6 nm)
Theory (L = 52.1 nm)
Mobility (cm²/Vs)
100
10
Dislocation and Neutral Impurity Scattering
GBS
Ionized Impurity Scattering
Ionized Impurity Cluster Scattering
Dislocation and Neutral Impurity Scattering
Dislocation and Neutral Impurity Scattering
(d)
(e)
(f)
IR
NIR-VIS-UV
$N_{opt} = N_{sim}$
'Optical' Carrier Concentration (cm⁻³)
Detection Limit (IR)
NIR Tailing
GBS
Carrier Concentration (cm⁻³)
10¹⁷
10¹⁸
10¹⁹
10²⁰
10²¹

Figure 2

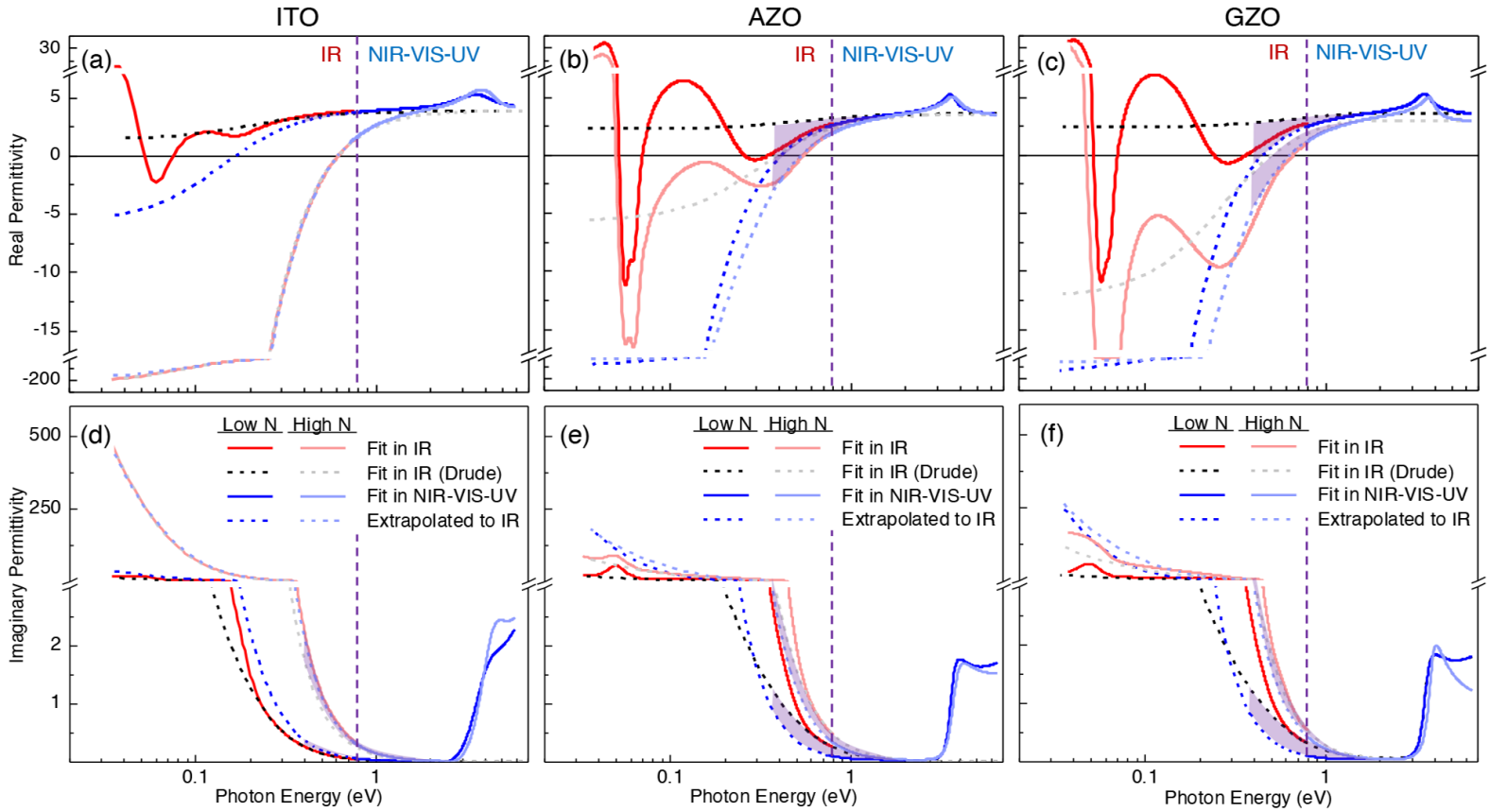
ITO
AZO
GZO
(a)
(b)
(c)
IR
NIR-VIS-UV
Real Permittivity
30
5
0
-5
-10
-15
-200
(d)
(e)
(f)
Low N
High N
Fit in IR
Fit in IR (Drude)
Fit in NIR-VIS-UV
Extrapolated to IR
Imaginary Permittivity
500
250
2
1
0.1
1
Photon Energy (eV)

Figure 3

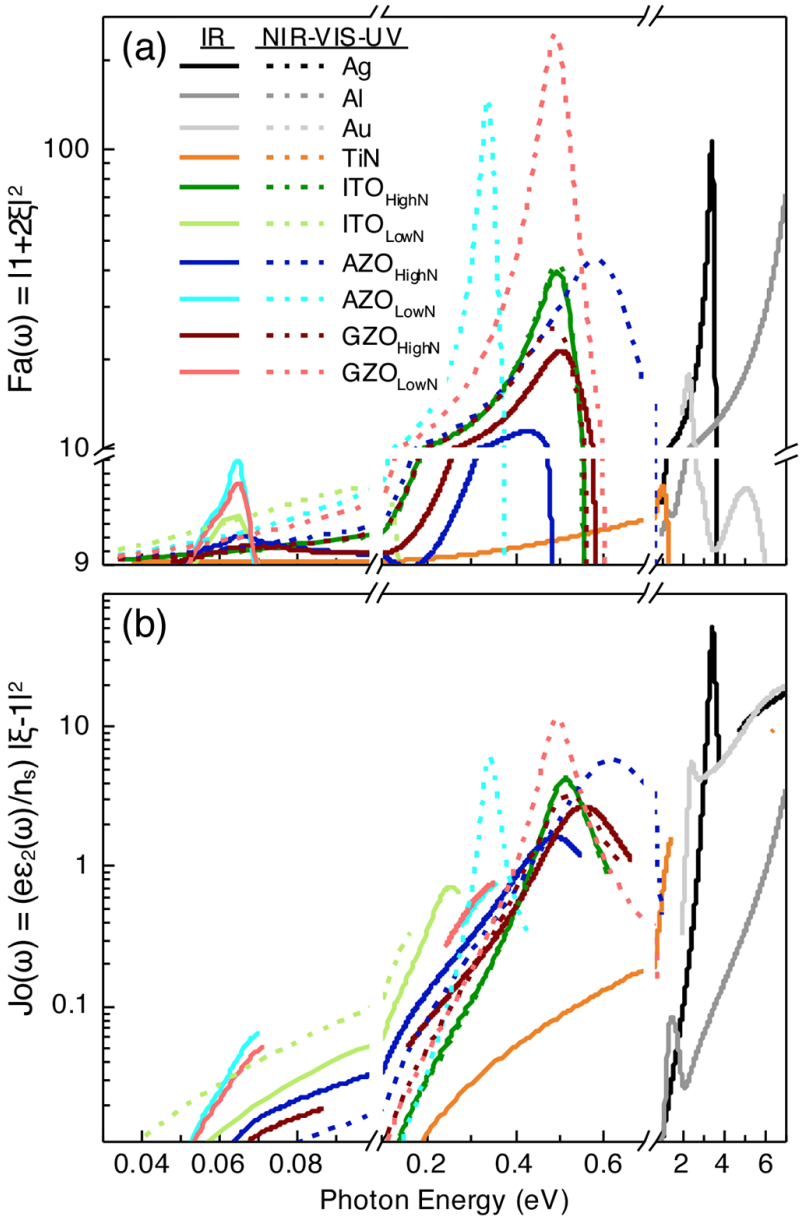
(a)
IR
NIR-VIS-UV
Ag
Al
Au
TiN
ITO HighN
ITO LowN
AZO HighN
AZO LowN
GZO HighN
GZO LowN
Fa(ω) = |1+2ξ|²
100
10
9
(b)
Jo(ω) = (eε₂(ω)/nₛ) |ξ-1|²
10
1
0.1
0.04
0.06
0.08
0.2
0.4
0.6
2
4
6
Photon Energy (eV)

For Table of Contents Only

When Ellipsometry Works Best - A Case Study With Transparent Conductive Oxides.

James A. Hillier, Sophie Camelio, Wayne Cranton, Alexei Nabok, Christopher J. Mellor, Demosthenes C. Koutsogeorgis, and Nikolaos Kalfagiannis[*]

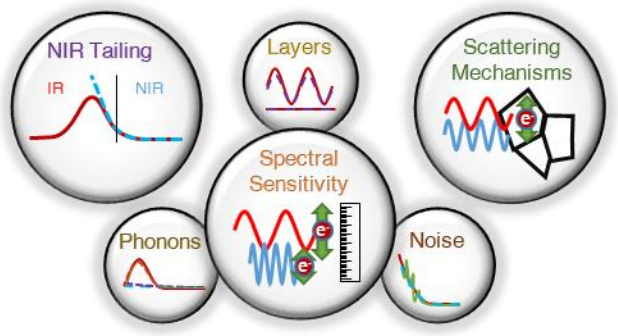

The graphic represents the different cases which are essential concerning the limitations of ellipsometry to determine the parameterized oscillators defining the optical constants of materials.